Laser multiple filamentation control in air using a smooth phase mask

P. Rohwetter, M. Queißer, K. Stelmaszczyk, M. Fechner, and L. Wöste
Institut für Experimentalphysik, Freie Universität Berlin, Arnimallee 14, 14195 Berlin, Germany
(Received 27 August 2007; published 15 January 2008)

We report on experimental results revealing the important role of linear diffraction in multiple filamentation of intense laser pulses propagating in air. We show that during the early stages of propagation the transverse energy redistribution is governed by the laws of classical optics, defining the initial conditions for subsequent filamentary breakup of the beam. This is done by introducing a smoothly varying transverse phase, resulting in deterministic multiple filamentation. The observations presented here indicate precise wave-front shaping as a way to control the highly nonlinear and otherwise turbulent aforesaid process, which is a prerequisite for a number of applications.

DOI: 10.1103/PhysRevA.77.013812 PACS number(s): 42.65.Jx, 42.65.Sf, 42.65.Re

Filamentation of high-power laser light is a ubiquitous phenomenon observed in various transparent nonlinear media. It is initiated by Kerr-lens-induced self-focusing collapse. As calculated numerically by Marburger and Dawes [1], a Gaussian cw laser beam of sufficiently high power will eventually contract to a small spot after propagating the self-focusing distance z_f [2],

$$z_f = 0.367 \frac{2\pi a_0^2}{\lambda} \{[(P/P_{\mathrm{crit}})^{1/2} - 0.852]^2 - 0.0219\}^{-1/2}, \quad (1)$$

where λ is the laser wavelength, a_0 is the initial beam radius at the waist at $z=0$, and P_{crit} is the critical power for self-focusing. In air and for wavelengths around 800 nm, $P_{\mathrm{crit}} \simeq 3.2$ GW [3]. Equation (1) provides a good approximation also in the case of ultrashort pulsed laser beams [3], which are most frequently used in filamentation experiments.

If the pulse power is equal to (or moderately exceeds) P_{crit}, a single filament on the beam axis is formed. This type of filament has been observed in experiments for many years [4] and is well predicted by numerical simulations using the extended nonlinear Schrödinger equation (see, for example, [5]). For much higher pulse powers (at least one or two orders of magnitude larger than P_{crit}), not only single but multiple filamentation (MF), i.e., creation of many filaments, is likely to occur.

High-power laser beams of many critical powers with noisy transverse profiles typically break up into randomly distributed filaments. This process is governed by noise amplification due to modulational instability [6] and turbulence [6,7], which randomizes not only transverse positions but also onset distances and relative energy content of individual filaments. In the case of pulsed lasers there is substantial shot-to-shot fluctuation of these quantities.

The random nature of MF can be suppressed in various ways. Dubietis *et al.* [8] and Fibich *et al.* [9] showed that an elliptically shaped laser beam undergoes MF in a predictable way. By introducing strong astigmatism, Méchain *et al.* [10] were able to create two stable filaments in the sagittal plane of a laser beam in air. Furthermore, they proposed to use various amplitude masks to regularize the distribution of filaments. Corsi *et al.* [11] transformed the transverse intensity modulation resulting from the interference of two laser pulses into a one-dimensional array of collinearly propagating filaments in glass. Schroeder *et al.* [12] and Kandidov *et al.* [13] used regular amplitude masks to create two-dimensional filament microarrays in liquids.

Recent numerical studies by Roskey *et al.* [14] have shown that linear diffraction can dominate the initial phase of propagation of apertured high-power beams, even if these undergo MF during further propagation. From their results they concluded that in general the transverse energy redistribution in the laser beam is due to linear diffraction just up to the moment when local supercriticality occurs, initiating local self-focusing collapse. They were able to predict MF patterning and approximate relative filament energies, as obtained from nonlinear simulation, from the results of simple linear numerical propagation. The proposed mechanism holds for a number of aperture geometries and laser powers and was termed linear power partitioning (LPP).

The purpose of the work presented in the following is to give experimental evidence of the importance of LPP for multiple filamentation in air. We show that predictable, transversally regular MF patterns can be obtained by diffractive LPP using a smooth reflective phase mask. We further show that transverse equipartitioning of laser energy controls and to some extent equalizes filamentation onset distances, a key parameter in many applications.

At the high laser powers necessary to induce filamentation in air, amplitude masks and transmitted phase masks have certain drawbacks. Amplitude masks are in practice restricted to discontinuous, shaped apertures, such as diaphragms or meshes that were used in [10,13]. By definition, these block energy from the beam and the sharp edges lead to large-angle diffraction. Transmitted phase masks, on the other hand, entail possible spatiotemporal pulse distortion by stretching through group-velocity dispersion, angular dispersion due to refraction, and unwanted strong nonlinear effects in the solid, possibly leading to permanent damage.

A numerical study by Panov *et al.* [15] examines the case of a phase mask made up of identical focusing lenslets aligned on a regular grid on a plane substrate. Their calculations of nonlinear laser pulse propagation show that, in order to eliminate the deterioration caused by air turbulence on filamentation pattern stability, the fill factor of this lens array should not be smaller than a certain threshold. In the same paper the authors stress that, in the case of phase masks also,

discontinuities of the complex pupil function should be avoided in order to minimize large-angle diffraction, which otherwise would reduce the advantage over amplitude masks.

In other words, the transverse spatial spectrum of the phase mask should contain only the lowest possible frequencies necessary to obtain the desired result while maximizing the "active" area of the phase mask.

These considerations lead to a smooth reflective phase mask as the preferred candidate for investigating MF in air. Its purpose of partitioning a centimeter-diameter laser beam into some tens of regularly patterned supercritical areas requires a corresponding dominant transverse spatial frequency of the phase modulation, while phase shifts should be on the order of single wavelengths. While conventional deformable mirrors are usually designed for lower-frequency wave-front correction, the present task seems to be principally achievable using a suitably modified microelectromechanical system spatial light modulator [16]. However, for simplicity, we resort to a less sophisticated though effective setup, relying on stationary, self-organizing "Faraday waves" [17,18] on the parametrically driven surface of a liquid. Synchronizing these with respect to the laser pulse train makes the oscillating reflective liquid surface a quasistatic, smoothly and regularly modulated spatial light modulator—a strobed dynamic deformable mirror (SDDM).

Faraday waves emerge once a critical amplitude of parametric forcing is overcome. The lowest-frequency modes to become unstable oscillate at half the driving frequency [17]. Strikingly, under very general conditions and just above the formation threshold, nonlinear coupling between unstable modes leads to the selection of regular or quasiregular patterns. Pattern selection is sensitive to parameters such as the drive frequency and amplitude, but also to fluid properties [18]. In the idealized case of an infinite liquid surface, the time-independent part of a regular standing Faraday wave pattern can be expanded as

$$h_0(\boldsymbol{r}) = \sum_m B_m \cos(\boldsymbol{k}_m \cdot \boldsymbol{r}), \tag{2}$$

where B_m are real amplitudes, $\boldsymbol{r}=(x,y)$ is the two-dimensional position vector, and $\boldsymbol{k}_m$ are the wave vectors in the x-y plane forming a regular polygon [18]. Finite containers with nonideal boundary conditions (such as a possibly nonuniform meniscus) are more complicated to handle. In contrast to exact circles or squares they often lack classical "integrability" [19], which complicates theoretical treatment and usually corrupts strict global regularity of the self-organized wave pattern. However, even under such conditions, the observed wave patterns can be very regular in certain domains of the surface (see, for example, Fig. 5(d) in [19]). This is the type of quasiregularity exhibited by the surface wave patterns we are able to produce with our SDDM and which we imprint on the transverse phase of the incident laser beam. Justified by the observation of local regularity, we use Eq. (2) for describing the surface height profile at the local spot illuminated by the laser, while relaxing the requirements on the $\boldsymbol{k}_m$. In other words, in the case discussed later on we drop the constraint on the $\boldsymbol{k}_m$ to have equal moduli and allow for a slight tilt angle between the two of them. This seemingly arbitrary procedure, however, leads to good agreement with our observations.

We chose gallium (Ga) as the material for our SDDM. Ga and some of its alloys have been previously used as liquid mirrors in astronomical optical systems [20]. In the spectral range of interest here, Ga has a reflectivity of 90% [21], which is about 13% higher than that of mercury, another potential SDDM material, which is less attractive due to its toxicity. The casing of the SDDM had a circular layout of 50 mm diameter and was made of polytetrafluoroethylene (PTFE). The base of the casing consisted of an elastic latex membrane that could be depressed by employing negative pressure. This enabled compensation of the otherwise strong convex meniscus of the liquid Ga, yielding a flat unmodulated SDDM. The surface of the SDDM was excited by a vibrating PTFE ring forming its boundary. A modified loudspeaker driver was used to vibrate the ring vertically at an exactly phase-locked multiple of the laser repetition rate of 10 Hz.

A commercial CPA Ti:Sapphire amplifier system delivered pulses of 801 nm, 120 fs duration and typically 1 or 30 mJ pulse energy. In situations when quasilinear propagation over the whole observed distance was necessary, low-energy pulses were used, while high-energy pulses of multiple critical powers ($P/P_{\mathrm{crit}} \simeq 80$) underwent multiple filamentation.

During adjustment, images of the transverse intensity distribution after reflection off the SDDM's surface and linear propagation along some distance were captured from a screen using a charge-coupled device camera. Impacts of high-power pulses were recorded on photographic paper (Ilford Multigrade IV). As was observed, filaments contained within the beam profile caused very distinctive, localized spots of ablation of the photographic paper's surface. The occurrence of such spots of ablation was checked to be strictly linked to the presence of a filament, as inferred from visible supercontinuum generation [3]. During SDDM setup the drive amplitude was increased from zero just up to the threshold of surface wave pattern formation. If needed, coupling between the driving PTFE ring and the surface was fine-tuned by adjusting its neutral z position with a micrometer screw. Above threshold it was then possible to influence the amplitude of surface modulation by varying the drive amplitude. To reliably achieve controlled MF within the available propagation distance, the modulation amplitude was set to produce a high-contrast diffraction pattern at a propagation distance of about $z_{\mathrm{contr}}=2.6$ m after the SDDM.

This pattern is next used to retrieve an approximate height profile by comparing the measured intensity distribution with calculated beam profiles obtained from numerical linear propagation of the phase-modulated laser beam. The true height profile $h(\boldsymbol{r})$ of the SDDM surface is approximated by the parametrization $\tilde{h}(\boldsymbol{r};\boldsymbol{k}_m,B_m)$, having the same form as $h_0(\boldsymbol{r})$ in Eq. (2). Local wave vectors $\boldsymbol{k}_m$ are chosen so as to produce the observed symmetry of the diffraction pattern. Treating the regularly modulated mirror surface as an array of small concave spherical mirrors with a focal length of $f=z_{\mathrm{contr}}$ leads to a first guess of the amplitudes B_m.

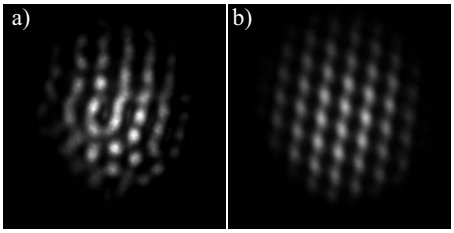

FIG. 1. Intensity distribution at $z=2.6$ m, (a) measured and (b) calculated for the specific parameter values given in the text. The actual side length of the square subimages is 25.6 mm.

The theoretical intensity distribution $I(\boldsymbol{r};z)$ at distance z from the model SDDM is calculated using the angular spectrum method [22]

$$I(\boldsymbol{r};z) = |\mathcal{F}^{-1}\{\mathcal{F}[U(\boldsymbol{r};0)]e^{i2\pi z\sqrt{1/\lambda^2-f_X^2-f_Y^2}}\}|^2, \tag{3}$$

where $U(\boldsymbol{r};0)=A_0(\boldsymbol{r})\exp\{i[\phi(\boldsymbol{r})+\Delta\phi(\boldsymbol{r})]\}$ is the complex amplitude of the laser field at $z=0$, $\mathcal{F}$ denotes Fourier transform into the transverse spatial frequency domain with coordinates (f_X,f_Y), and $\mathcal{F}^{-1}$ is its inverse. At normal incidence the imposed phase shift due to reflection on the model SDDM is given by

$$\Delta\phi(\boldsymbol{r}) = -\frac{4\pi}{\lambda}\tilde{h}(\boldsymbol{r};\boldsymbol{k}_m,B_m) + \frac{\pi}{\lambda f}|\boldsymbol{r}|^2 + \pi, \tag{4}$$

where the first term describes the local phase shift due to the model SDDM height profile, the second term models slight overall focusing or defocusing with focal length f due to residual global curvature, and the third is the phase shift of π due to reflection. The most probable approximate height profile is obtained by iteratively adjusting the $\boldsymbol{k}_m$ and B_m to reproduce as closely as possible the observed diffraction pattern at various distances.

We now consider a particular example where the SDDM was driven at 100 Hz, resulting in a standing Faraday wave pattern of local rhombic symmetry. The function describing the surface height profile at the arrival times of the laser pulses was approximated as

$$\tilde{h}(\boldsymbol{r}) = \frac{B}{3}\{2\cos[\boldsymbol{k}_1\cdot(\boldsymbol{r}-\Delta\boldsymbol{r})] + \cos[\boldsymbol{k}_2\cdot(\boldsymbol{r}-\Delta\boldsymbol{r})]\} \tag{5}$$

with $|\boldsymbol{k}_1|=|\boldsymbol{k}_2|=2900\ \mathrm{m}^{-1}$; $B=47.7$ nm; $\Delta\boldsymbol{r}$ is a nondescript spatial offset; $\angle(\boldsymbol{k}_1,\boldsymbol{k}_2)=70°$. The global focal length in the second term of Eq. (4) was set to $f=-15$ m, corresponding to slight overall divergence.

In Fig. 1 the measured (a) and calculated (b) intensity distribution across the laser beam are shown for $z=2.6$ m. Insignificance of nonlinear effects is guaranteed under the present low-power conditions (1 mJ pulse energy), where even the most intense hotspots stay below $P<0.04P_{\mathrm{crit}}$. Inspection shows that the approximation $\tilde{h}(\boldsymbol{r})$ consisting of a superposition of just two plane waves leads to good agreement between the measured and synthesized intensity profiles. A distinctive and orderly distribution of "islands" of high intensity is clearly apparent in both images. The same good agreement was found throughout the accessible propagation range, confirming the suitability of the chosen set of parameters.

In the following we show that linear diffraction in the initial stage of propagation determines the intensity profile of the nonlinearly propagating beam. To confirm this, the same transverse phase pattern was imposed on the laser beam, while the pulse energy was increased to 30 mJ. As before, Fig. 2 presents measured and calculated beam profiles, here for the highly nonlinear case. Each column consists of an image of a beam impact on photographic paper obtained at a distance z from the SDDM (above), and the numerically linearly propagated, phase-modulated input beam at the same distance (below). The impact images have been background corrected and slightly denoised with a Gaussian filter.

As can be seen from the upper row of Fig. 2 together with Fig. 3, where the life spans of individual filaments are visualized, the nonlinearly propagating beam develops an array

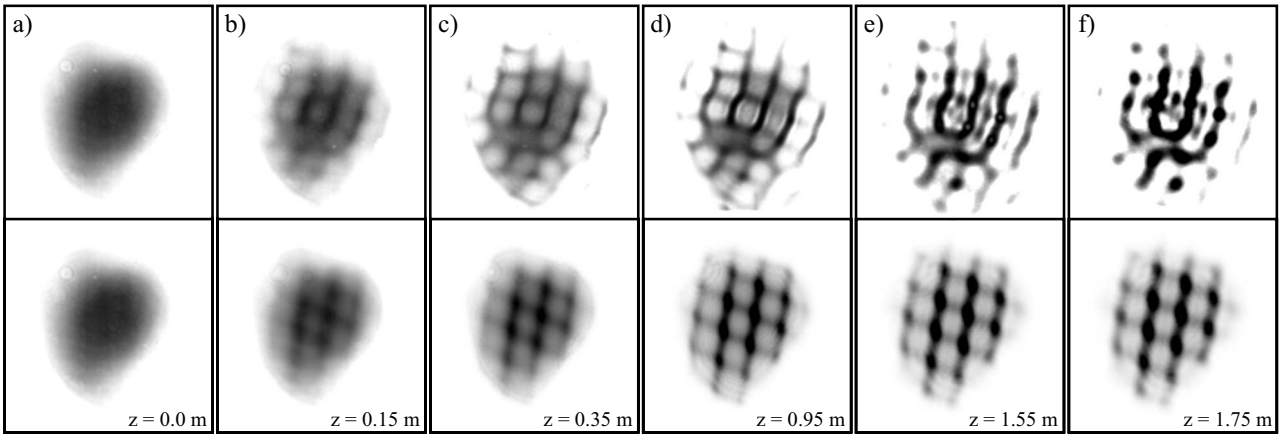

FIG. 2. Comparison of measured beam impacts (upper) and calculated intensity distributions (lower) as obtained from linear propagation of the beam. (a)–(f) correspond to propagated distances z of 0.0, 0.15, 0.35, 0.95, 1.55, and 1.75 m. The imposed phase pattern is the same as in Fig. 1. The actual side length of the square subimages is 15.9 mm. The gray scale of the calculated profiles is inverted for better visual comparability.

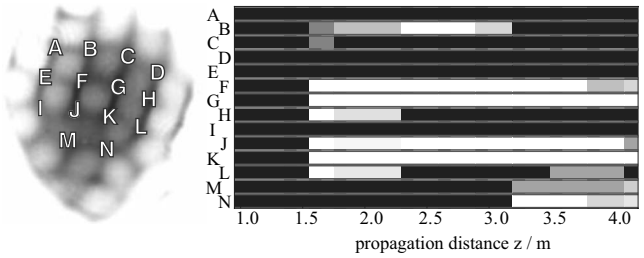

FIG. 3. Filament life spans for the most intense hotspots. The gray scale visualizes the per shot probability of detecting a filament (white: probability of occurrence equal to 1). The naming convention is defined on the left [compare to Fig. 2(c)].

of quasiregularly organized hotspots, most of which eventually undergo filamentation within the observed distance of about 4 m. Remarkably, the pattern is very similar to that obtained at low power. Hotspots *B*, *C*, *F*, *G*, *H*, *J*, *K*, and *L* almost simultaneously form filaments at about $z=1.55$ m. The high-intensity features that later on form veritable hotspots already emerge as faint modulations of the intensity profile at $z=0.15$ m. Even at this early stage of propagation, the pattern of future beam breakup can be anticipated.

The lower row of Fig. 2 shows the corresponding synthetic beam profile resulting from numerical linear propagation of the same initial intensity profile. As before, the phase was modulated according to Eqs. (4) and (5). The qualitative agreement of both the measured and calculated beam profiles is apparent throughout the propagated distance. Clearly, LPP structures the intensity profile before nonlinear self-focusing kicks in and filaments develop according to the prescribed pattern. From the calculated beam profile Fig. 2(b), one can infer that, at this stage, the contrast of the induced intensity modulations with respect to the local average intensity is still just on the order of a percent. At the same time each of them together with its respective environment is substantially supercritical in terms of self-focusing. Intensity gradients are, however, still gentle, leading to weak net local Kerr lensing. During further quasilinear propagation, energy is increasingly concentrated in the developing hotspots until, at about [Fig. 2(d)] $z=0.95$ m, linear diffraction has led to a high-contrast, patterned beam profile. Hotspots are distinctly separated from each other, but filamentary collapse has not yet occurred in any of them (see Fig. 3). The main prerequisites for the application of Eq. (1) are satisfied, and we use it for an approximate consistency check. Not considering local wave-front curvature, from the calculated profile [Fig. 2(d)] one finds prospective self-focusing distances z_f in the range $0.4\ \text{m} \leqslant z_f \leqslant 1.3$ m, corresponding to $1.3 \leqslant z \leqslant 2.2$ m from the SDDM. For the more intense hotspots *B*, *C*, *F*, *G*, *H*, *J*, *K*, *L*, this range reduces to $1.3 \leqslant z \leqslant 1.7$ m. Indeed, at [Fig. 2(e)] $z=1.55$ m the eight more intense hotspots have undergone filamentation, most notably at virtually the same propagation distance between $z=1.35$ and 1.55 m, consistent with the estimate from [Fig. 2(d)] $z=0.95$ m. Considering the rather subjective choice of the distance where collapse is assumed to be initiated, this close match, however, must not be overrated. Apparently the linearly propagating beam scarcely changes shape between $z=1.55$ m and [Fig. 2(f)] $z=1.75$ m, while in the real beam one observes continuing concentration of energy in the hotspots, indicating ongoing self-focusing. This is consistent with the obvious fact that linear diffraction theory breaks down once self-action sets in.

In the present case, four of the initially eight simultaneously formed filaments survive up to $z=4.09$ m, the farthest possible distance available in the laboratory, while hotspots *M* and *N* actually produce filaments only beyond $z \simeq 3$ m. The filament in hotspot *L* remarkably experiences a revival at $z \simeq 3.5$ m. The spread of self-focusing distances and, even more, of the filament lifetimes seems to be mainly caused by the inhomogeneous partition of the laser energy among the hotspots. This effect is included even in our rough estimate of filamentation onset distances. Due to the regularity of the phase pattern and the assumed linear propagation, the shapes, and from this the beam parameter a_0 that enters Eq. (1) in our estimation, are virtually the same for all hotspots. For this reason the estimated filamentation onset distance is mainly determined by the placement of the corresponding hotspot within the original beam profile, as is experimentally observed. The central hotspots *F*, *G*, *J*, and *K* form the most persistent filaments. Their simultaneous onset distances reflect the fact that their precursory hotspots resemble each other in shape and energy content, as they symmetrically share the central part of the beam. Comparison of the approximate powers of these central hotspots that enter Eq. (1), and that are obtained from the Gaussian fits to the individual hotspots in the linearly calculated profile at [Fig. 2(d)] $z=0.95$ m, confirms the visual impression. The relative powers there are (0.9, 1.0, 0.9, 0.9) for hotspots (F,G,J,K), respectively, hotspot *G* enclosing slightly more intensity. The relatively delayed filamentation of hotspots *M* and *N* is likely to be caused by their lower energy content and the longer self-focusing distance resulting therefrom. However, in this case, the simple estimation yields as prospective absolute self-focusing distances $z_M \simeq 1.6$ m and $z_N \simeq 1.9$ m from the SDDM. Inspection of Figs. 2(d) and 2(f) indicates that, due to the worsening agreement of the model with the real SDDM pattern in the lower part of the beam profile, these estimates are to be doubted in this case. A perfect control of the transverse phase would be needed here to allow for a more reliable test of the asserted effect.

Nonetheless, our observations indicate the importance of energy partition among the linearly seeded hotspots generated by transverse phase modulation. Numerical results by Panov *et al.* [15] show that energy equipartition is a key factor for synchronizing the longitudinal onset distances in a bunch of filaments. Their nonlinear calculations of beam propagation show that one can expect synchronous onset of filamentation, if the energy content *and* size (at a particular propagation distance) of individual local hotspots can be independently and simultaneously controlled. They propose a concentric arrangement of circular lenslets with radii adapted to enclose equal amounts of laser energy, and with individual focal lengths optimized for simultaneous filament formation. In terms of LPP and in view of Eq. (1) this would mean adaption of the phase mask to induce formation of separated hotspots *n* with individual powers P_n and beam parameters $a_{0,n}(z_n)$ at the propagation distances z_n where filamentary collapse is initiated, so that

$$z_n + z_{f,n} = z_{\mathrm{FO}} \quad \text{for all hotspots } n, \quad \text{where}$$

$$z_{f,n} = z_f(a_{0,n}(z_n), P_n), \tag{6}$$

$z_f(a_0, P)$ is defined according to Eq. (1), and z_{FO} denotes the common absolute propagation distance to filament onset. This type of full phase control is beyond the capabilities of our simple SDDM. However, our results suggest that, should this control be available, linear diffraction can indeed serve to predict and control filamentation in air. This is meant in the following sense: Given a desired spatial filamentation pattern plus the original transversal beam profile, a simple and quick linear calculation can serve to draft a phase mask that creates a corresponding intensity profile at some propagation distance that is prone to multiple filamentation according to simplified criteria, as for example the ones in Eq. (6). Iterative optimization (as, for example, numerically done in [15]) could then follow for improved results.

Reconsideration of the life spans (see Fig. 3) of the "equivalent" central filaments formed from their precursory hotspots *F*, *G*, *J*, and *K* seems to corroborate an assumption stated in [15], that energy equipartition among the latter should equalize the propagated distances through which the associated filaments survive.

Finally, to come back to the experiment, we note that the unmodulated beam actually did not undergo spontaneous filamentation at all within the observed distance.

Summarizing, we have shown that linear diffraction plays a crucial role during the early stages of propagation of intense laser beams in air. This can serve to introduce considerable determinism into the otherwise turbulent process of multiple filamentation, as we have demonstrated by organizing multiple filamentation using a reflective phase mask. The present proof of principle urges the next step, i.e., the development of a dedicated, fully controlled spatial light modulator based on existing technology [16] and its application in the field of filamentation in air.

[1] J. H. Marburger and E. L. Dawes, Phys. Rev. Lett. **21**, 556 (1968).
[2] Y. R. Shen, *The Principles of Nonlinear Optics* (Wiley, New York, 1984).
[3] A. Couairon and A. Mysyrowicz, Phys. Rep. **441**, 47 (2007).
[4] A. Braun, G. Korn, X. Liu, D. Du, J. Squier, and G. Mourou, Opt. Lett. **20**, 73 (1995).
[5] A. Couairon and L. Bergé, Phys. Rev. Lett. **88**, 135003 (2002).
[6] L. Bergé, S. Skupin, F. Lederer, G. Méjean, J. Yu, J. Kasparian, E. Salmon, J. P. Wolf, M. Rodriguez, L. Wöste, R. Bourayou, and R. Sauerbrey, Phys. Rev. Lett. **92**, 225002 (2004).
[7] M. Mlejnek, M. Kolesik, J. V. Moloney, and E. M. Wright, Phys. Rev. Lett. **83**, 2938 (1999).
[8] A. Dubietis, G. Tamosauskas, G. Fibich, and B. Ilan, Opt. Lett. **29**, 1126 (2004).
[9] G. Fibich, S. Eisenmann, B. Ilan, and A. Zigler, Opt. Lett. **29**, 1772 (2004).
[10] G. Méchain, A. Couairon, M. Franco, B. Prade, and A. Mysyrowicz, Phys. Rev. Lett. **93**, 035003 (2004).
[11] C. Corsi, A. Tortora, M. Bellini, Appl. Phys. B: Lasers Opt. **78**, 299 (2004).
[12] H. Schroeder, J. Liu, S. Chin, Opt. Express **12**, 4768 (2004).
[13] V. P. Kandidov, N. Akozbek, M. Scalora, O. G. Kosareva, A. V. Nyakk, Q. Luo, S. A. Hosseini, and S. L. Chin, Quantum Electron. **34**, 879 (2004).
[14] D. E. Roskey, M. Kolesik, J. V. Moloney, and E. M. Wright, Appl. Phys. B: Lasers Opt. **86**, 249 (2007).
[15] N. A. Panov, O. G. Kosareva, and I. N. Murtazin, J. Opt. Technol. **73**, 778 (2006).
[16] T. Bifano, P. A. Bierden, H. Zhu, S. Cornelissen, and J. H. Kim, Proc. SPIE **5490**, 1472 (2004).
[17] M. C. Cross and P. C. Hohenberg, Rev. Mod. Phys. **65**, 851 (1993).
[18] P. Chen and J. Viñals, Phys. Rev. Lett. **79**, 2670 (1997).
[19] A. Kudrolli, M. C. Abraham, and J. P. Gollub, Phys. Rev. E **63**, 026208 (2001).
[20] E. F. Borra, G. Tremblay, Y. Huot, and J. Gauvin, Publ. Astron. Soc. Pac. **109**, 319 (1997).
[21] L. G. Schulz, J. Opt. Soc. Am. **47**, 64 (1957).
[22] J. W. Goodman, *Introduction to Fourier Optics* (McGraw-Hill, San Francisco, 1968).